Hindawi
Journal of Electrical and Computer Engineering
Volume 2019, Article ID 1469637, 11 pages
https://doi.org/10.1155/2019/1469637

Research Article

An Analytical Solution to the Electromagnetic Performance of an Ultra-High-Speed PM Motor

Wenjie Cheng,[1] **Zhikai Deng**,[1] **Ling Xiao**,[1] **Bin Zhong**,[2] **and Yanhua Sun**[3]

[1]*College of Science, Xi'an University of Science and Technology, No. 58, Yanta Road, Xi'an, China*
[2]*School of Mechanical Engineering, Xi'an University of Science and Technology, No. 58, Yanta Road, Xi'an, China*
[3]*State Key Laboratory for Strength and Vibration of Mechanical Structures, Xi'an Jiaotong University, No. 28, Xianning West Road, Xi'an, China*

Correspondence should be addressed to Wenjie Cheng; cwj20070807@163.com

Received 21 February 2019; Revised 23 July 2019; Accepted 18 August 2019; Published 12 September 2019

Academic Editor: Gorazd Stumberger

Bipolar rotors with cylindrical permanent magnets (PMs), which are magnetized in parallel, are generally used in ultra-high-speed permanent magnet synchronous motors (PMSMs). Aiming for this type of PMSM, two methods, namely, the Poynting theorem and the Maxwell stress tensor, were used to deduce the analytic expression of the electromagnetic driving torque. A locked-rotor simulation by the finite element (FE) method verifies the analytical solution. In addition, the cogging torque, back-electromotive force (emf), armature reaction inductance, etc., were calculated, compared, and discussed. The no-load back-emf was checked by a 60,000 rpm free coast experiment. The proposed analytical solution is very convenient to guide the design of the ultra-high-speed PMSM and check its performance.

1. Introduction

With advancements in new materials, electrical and electronics, control technology, etc., the speed limits of rotating machines are being pushed higher, and ultra-high-speed motors are increasingly used in industry applications [1]. Particularly in recent times, the high-speed PMSM has attracted more attention due to its high efficiency, simple structure, high power density, and small size [2, 3]; for example, it can be used as the driving motor for the fuel cell air blower [4, 5], as an air centrifugal compressor [6], or as the generator of a micro-gas turbine [7].

It is very significant to calculate the electromagnetic torque, because it can be used to check the motor power, estimate noise and vibration, and provide further guidance for the motor control. It is well known that the electromagnetic torque is generated from the interaction of the PM field and the armature reaction field; therefore, how to determine the above two magnetic fields becomes key. PMSMs often adopt a surface-mounted PM rotor, and this kind of rotor, as seen in most relevant literatures [8, 9], has a common characteristic, which is that the magnetic pole arc is less than a pole pitch (the pole embrace is less than 1), which means the air space between the magnets is occupied by unmagnetized materials, such as air or aluminum alloy. Rotors of the ultra-high-speed PMSM are always subject to extreme conditions, such as high speed and high temperature. To improve the bending stiffness and strength of the rotor, ultra-high-speed PMSMs generally use a special rotor construction, in which a cylindrical PM magnetized in parallel is interference-fitted into a metallic sleeve; therefore, the rotor has single pole pairs, and each half of the magnet has a 180° electric pole arc (the pole embrace is equal to 1), as shown in Figure 1. As mentioned in the literature [10], existing analytical methods are successful only in certain circumstances and are likely to fail in others, for example, when the magnets have a 180° electric pole arc. In the literature [11] study, an open-circuit magnetostatic field solution to a 2-pole rotor with a diametrically magnetized sintered NdFeB magnet was given for a 20,000 rpm, 3-phase brushless PM dc motor. Recently, the literature [12]

gave analytical solutions to the PM field of bipolar rotors with ring or cylindrical PMs that are magnetized in parallel. Nevertheless, most relevant literature studies on analytical models for predicting the armature reaction field distribution are successful for the motor, owing to the high permeability shaft [13]; however, few studies involve the hollow stator bore as shown in Figure 2(b).

For ultra-high-speed PMSMs including a stator with overlapping windings and 2-pole parallel magnetized cylindrical PMs, analytical solutions to the magnetic field and corresponding electromagnetic torque are rarely reported at present, which has resulted in a prolonged motor design cycle to evaluating the motor performance. Due to the need of cooling and reduction of pulse torque, the ultra-high-speed PMSM generally adopts a large air gap; hereupon, the slot effect is very weak. Therefore, the assumption of "slotless stator + equivalent current sheet" can be introduced, and some convenient formulas of estimating motor performance are expected to be obtained.

Hence, this paper will first deduce the magnetic field, then obtain the electromagnetic driving torque by using the Poynting theorem and Maxwell stress tensor, and then verify the correctness by using the FE method. In addition, the cogging torque, the back-electromotive force (emf), and armature reaction inductance are calculated, compared, and discussed. A 10 kW, 120,000 rpm prototype is designed and manufactured, and the no-load back-emf is checked by a 60,000 rpm free coast experiment.

2. Analytical Model

The cross section of the ultra-high-speed PMSMs is shown in Figure 1, in which slotted stator and distribution winding are used, and the rotor is composed by installing a cylindrical parallel polarized PM into the metallic sleeve.

For the sintered NdFeB magnet, the demagnetization curve is approximately a straight line, and the relative recoil permeability μ_r is approximate to that of air. μ_r was chosen from 1.029–1.100 in most literatures. To simplify the field calculation, the following assumptions are made:

(1) The PM has a linear second-quadrant demagnetization curve, and the permeability of the stator iron is infinite

(2) The winding end effect and rotor eddy current are neglected

(3) The PM field is calculated with a 2D solution by assuming a smooth stator surface; that is, the slotting is neglected, as shown in Figure 2(a)

(4) Conductors in the stator slot can be equivalent to the current sheet distributing evenly along the slot opening, as shown in Figure 2(b)

In the calculation of the PM field, the slot-opening effect is neglected; therefore, the calculation model of the PM field is shown in Figure 2(a), where R_1 and R_2 are the outer radius and the inner radius of the PM, and I and II represent the PM and the air region, respectively.

The sleeve applies to a low permeability alloy, which can be physically equivalent to the air; therefore, in the calculation model of the armature reaction field, the stator bore seems to be full of air, as shown in Figure 2(b), where b_0 is the width of the slot opening.

The loaded magnetic field is the superposition of the open-circuit PM and the armature reaction field, and the loaded air-gap flux density is defined as follows:

$$\begin{cases} B_{\mathrm{II}r}^{\mathrm{load}} = B_{\mathrm{II}r}^{W} + B_{\mathrm{II}r}^{\mathrm{PM}}, \\ B_{\mathrm{II}\theta}^{\mathrm{load}} = B_{\mathrm{II}\theta}^{W} + B_{\mathrm{II}\theta}^{\mathrm{PM}}. \end{cases} \tag{1}$$

In equation (1), load, PM, and W represent the loaded, PM, and winding magnetic fields, respectively. r and θ represent the radial and circumferential directions, respectively.

2.1. Open-Circuit Magnetic Field. The literature [12] has deduced the solution to the PM field shown in Figure 2(a), which is given as follows:

$$\begin{aligned} B_{\mathrm{II}r}^{\mathrm{PM}} &= \frac{-\mu_0 M_r R_1^2 \left(1 + R_2^2 r^{-2}\right)}{R_1^2 \left(\mu_r - 1\right) - R_2^2 \left(\mu_r + 1\right)} \cos\theta, \\ B_{\mathrm{II}\theta}^{\mathrm{PM}} &= \frac{\mu_0 M_r R_1^2 \left(-1 + R_2^2 r^{-2}\right)}{R_1^2 \left(\mu_r - 1\right) - R_2^2 \left(\mu_r + 1\right)} \sin\theta, \end{aligned} \tag{2}$$

where M_r is the amplitude of the residual magnetization of the PM, μ_r is the relative recoil permeability of the PM, μ_0 is the vacuum permeability, and r and θ represent the radial and circumferential positions, respectively.

2.2. Armature Reaction Field. The governing equation of the air-gap region is as follows:

$$\frac{\partial \phi^2}{\partial^2 r} + \frac{\partial \phi}{r \partial r} + \frac{\partial \phi^2}{r^2 \partial \theta^2} = 0, \tag{3}$$

where ϕ is a scalar magnetic potential, and the relation of ϕ and H (magnetic field intensity) is expressed as follows:

$$\begin{cases} H_\theta = -\dfrac{\partial \phi}{r\, \partial \theta}, \\ H_r = -\dfrac{\partial \phi}{\partial r}. \end{cases} \tag{4}$$

In the inner radius of the stator,

$$H_\theta \big|_{r=R_2} = -J, \tag{5}$$

where J is the Fourier series expansion of the current sheet. At the center of the stator, the H should meet the following:

$$\begin{aligned} H_\theta \big|_{r \longrightarrow 0} &\neq \infty, \\ H_r \big|_{r \longrightarrow 0} &\neq \infty. \end{aligned} \tag{6}$$

Taking into account the symmetry of the magnetic field, the single conductor field can be solved according to equations (3)–(6). The method to solve the armature

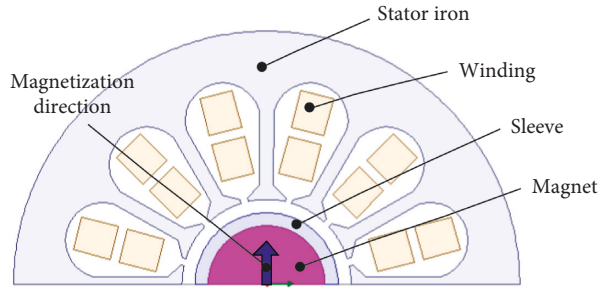

Figure 1: Cross section of the ultra-high-speed PMSM.

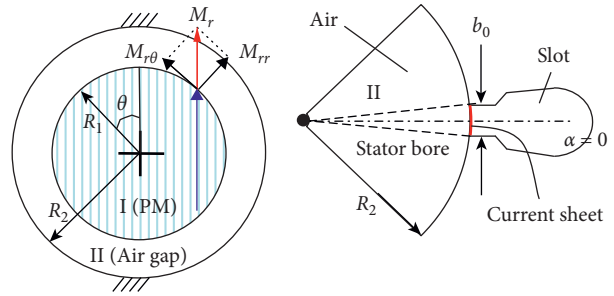

Figure 2: Models of the electromagnetic field of the PMSMs. (a) Open-circuit PM field. (b) Armature reaction field.

reaction field is as follows: the single conductor field is solved first, and then the single-turn coil field can be obtained by adding two single conductor fields at a polar distance apart from each other. Whereupon, the single-phase winding field is superpositioned onto fields that are excited by the multiple single-turn coils, and finally, the armature reaction field can be calculated by superimposing the fields of three-phase winding.

For distributed winding, multiple single-turn coil fields that are a pitch apart from each other can be equivalent to a concentrated winding by taking into account the distribution coefficient and the pitch-shortening coefficient. The above-mentioned treatment will lightly change higher harmonic components of the armature reaction field but vastly simplify the solution of the single-phase winding field with good accuracy. In addition, it is assumed that instantaneous three-phase currents (i_a, i_b, i_c) only involve fundamental components, and they can be written as follows:

$$\begin{cases} i_a = I_m \cos(P\omega t + \beta), \\ i_b = I_m \cos\left(P\omega t + \beta - \dfrac{2\pi}{3}\right), \\ i_c = I_m \cos\left(P\omega t + \beta - \dfrac{4\pi}{3}\right), \end{cases} \tag{7}$$

where I_m is the current amplitude of a single conductor, P is the number of pole pairs, ω is the synchronous angular velocity, and β is the current phase.

The armature reaction field in Figure 2(b) is expressed as follows:

$$\begin{aligned} B_{\mathrm{II}r}^{W} = {} & \frac{-2qN_s\mu_0}{\pi} \sum_{v=1}^{\infty} \Bigg\{ K_{\mathrm{dpv}}(2v-1) K_{\mathrm{sov}}(2v-1) \\ & \cdot F_o(2v-1, r) \cdot (-1)^v \cdot \Bigg[i_a \cos[(2v-1)(\alpha-\gamma)] \\ & + i_b \cos\left[(2v-1)\left(\alpha-\gamma-\frac{2\pi}{3}\right)\right] \\ & + i_c \cos\left[(2v-1)\left(\alpha-\gamma-\frac{4\pi}{3}\right)\right] \Bigg] \Bigg\}, \\ B_{\mathrm{II}\alpha}^{W} = {} & \frac{-2qN_s\mu_0}{\pi} \sum_{v=1}^{\infty} \Bigg\{ K_{\mathrm{dpv}}(2v-1) K_{\mathrm{sov}}(2v-1) \\ & \cdot F_o(2v-1, r) \cdot (-1)^{v-1} \cdot \Bigg[i_a \sin[(2v-1)(\alpha-\gamma)] \\ & + i_b \sin\left[(2v-1)\left(\alpha-\gamma-\frac{2\pi}{3}\right)\right] \\ & + i_c \sin\left[(2v-1)\left(\alpha-\gamma-\frac{4\pi}{3}\right)\right] \Bigg] \Bigg\}, \end{aligned} \tag{8}$$

where $K_{\mathrm{sov}}(v) = \sin(vb_0/(2R_2))/(vb_0/(2R_2))$ is the slot-opening coefficient, which is a function of the spatial harmonic order v. $F_o(r, v) = r^{v-1}/R_2^v$ reflects the influence of the air-gap thickness on the radial/circumferential flux density of the v order harmonic wave. α is the angle relative to the horizontal direction, as shown in Figure 2(b), and is positive

in the counter clockwise direction. γ is an angle between the axis of winding A and the d-axis. q is the number of slots per phase per pole, and N_s is the number of conductors per slot.

2.3. Electromagnetic Torque and Cogging Torque. In this part, two methods, namely, the Poynting theorem and the Maxwell stress tensor, were used to deduce the analytic expression of the electromagnetic torque. For the 2D field, the electric field strength vector E in the air-gap region only includes the axial component E_z; therefore, the Poynting vector is given by the following:

$$\begin{cases} \prod_r = -E_z H_\theta, \\ \prod_\theta = E_z H_r, \\ \prod_z = 0, \end{cases} \tag{9}$$

where $E_z = \mu_0 \int (\partial H_\theta / \partial t) dr$. The electromagnetic power transmitting from the stator to the rotor is mainly dependent on the radial component of the Poynting vector Π_r which can be calculated from equation (10) as follows:

$$P_M = T_{\text{em}}\omega = l_{\text{ef}} \int_0^{2\pi} \prod_r r \, d\theta, \tag{10}$$

where l_{ef} is the length of the stator iron. Taking the horizontal axis in Figure 2(b) as the reference position, the PM field is changed as follows:

$$\begin{aligned} B_{\text{II}r}^{\text{PM}} &= -\frac{\mu_0 M_r R_1^2 \left(1 + R_2^2 r^{-2}\right)}{R_1^2 (\mu_r - 1) - R_2^2 (\mu_r + 1)} \cdot \cos(\varphi), \\ B_{\text{II}\theta}^{\text{PM}} &= \frac{\mu_0 M_r R_1^2 \left(-1 + R_2^2 r^{-2}\right)}{R_1^2 (\mu_r - 1) - R_2^2 (\mu_r + 1)} \cdot \sin(\varphi), \end{aligned} \tag{11}$$

where $\varphi = \theta - \pi/2 = \alpha$. It is assumed that the electromagnetic power is mainly transmitted by the fundamental magnetic field of armature reaction field. When the number of pole pairs equals 1, by substituting equation (7) into equation (8), the armature reaction field will become as follows, using the properties of trigonometric functions:

$$\begin{aligned} B_{\text{II}r}^{W} &= \mu_0 G_1 \cos(\omega t - \varphi + \delta), \\ B_{\text{II}\theta}^{W} &= \mu_0 G_1 \sin(\omega t - \varphi + \delta), \end{aligned} \tag{12}$$

where $\delta = \beta + \gamma$ represents the angle between the axis of armature reaction field and the axis of PM field and $G_1 = (3qN_s K_{\text{dp1}} K_{\text{so1}} I_m)/(\pi R_2)$. Equation (12) shows that the armature reaction field is a travelling wave, but the PM field is a standing wave shown by equation (11). To make the PM field rotate counterclockwise synchronously relative to the armature reaction field, equation (11) can written as the following:

$$\begin{aligned} B_{\text{II}r}^{\text{PM}} &= \mu_0 \left(-G_2 r^{-2} - G_3\right) \cdot \cos(\varphi - \omega t), \\ B_{\text{II}\theta}^{\text{PM}} &= \mu_0 \left(G_2 r^{-2} - G_3\right) \cdot \sin(\varphi - \omega t), \end{aligned} \tag{13}$$

where $G_2 = M_r R_1^2 R_2^2 / [R_1^2 (\mu_r - 1) - R_2^2 (\mu_r + 1)]$ and $G_3 = M_r R_1^2 / [R_1^2 (\mu_r - 1) - R_2^2 (\mu_r + 1)]$. Therefore, the loaded gap magnetic intensity can be obtained as follows:

$$\begin{aligned} H_{\text{II}r} &= \left[G_1 \cos(\omega t - \varphi + \delta) + \left(-G_2 r^{-2} - G_3\right) \cdot \cos(\varphi - \omega t)\right], \\ H_{\text{II}\theta} &= \left[G_1 \sin(\omega t - \varphi + \delta) + \left(G_2 r^{-2} - G_3\right) \cdot \sin(\varphi - \omega t)\right]. \end{aligned} \tag{14}$$

Furthermore, E_z can be obtained by $H_{\text{II}\theta}$ and is expressed as the following:

$$E_z = \mu_0 \omega r \left[G_1 \cos(\omega t - \varphi + \delta) + \left(G_2 r^{-2} + G_3\right) \cos(\varphi - \omega t)\right]. \tag{15}$$

By substituting equation (15) into equation (9), Π_r will be calculated, and according to equation (10), the electromagnetic torque can be obtained as follows:

$$T_{\text{em}} = -2\pi \mu_0 l_{\text{ef}} G_1 G_2 \sin\delta, \quad \delta \in [0, \pi]. \tag{16}$$

In the 2D electromagnetic field, $f_\theta = B_r B_\theta / \mu_0$, and f_θ is the circumferential electromagnetic force density acting on the stator or rotor. Therefore, the electromagnetic torque of the rotor, which is shown in Figure 1, can be written as the following:

$$T_{\text{em}} = 2\mu_0 l_{\text{ef}} \int_0^{\pi} H_{\text{II}r} H_{\text{II}\theta} r^2 d\theta. \tag{17}$$

By substituting equation (14) into equation (17), the expression of the electromagnetic torque Tem is as follows:

$$\begin{aligned} T_{\text{em}} &= -2\pi \mu_0 l_{\text{ef}} G_1 G_3 r^2 \sin\delta, \quad \delta \in [0, \pi], \\ &\approx 6\pi \mu_0 q K_{\text{dp1}} K_{\text{so1}} \frac{N_s I_m}{2\pi R_2} \left(\frac{R_1}{R_2}\right)^2 M_r l_{\text{ef}} r^2 \sin\delta. \end{aligned} \tag{18}$$

In equation (18), when $r = R_2$, equation (18) is equal to equation (16), which indicates that the torque acting on the rotor surface generated by the Maxwell stress equals the torque acting on the current sheet generated by the ampere force. The results show that the electromagnetic torque is proportional to the length of stator iron l_{ef}, the ampere turns per unit length of the stator inner surface $N_s I_m / 2\pi R_2$, and the magnetization M_r, while it is proportional to the square of the ratio $(R_1/R_2)^2$ (PM radius to stator inner radius).

The cogging torque arises from the interaction of the magnetomotive force (mmf) harmonics and the airgap permeance harmonics; hence, it exists in almost all types of motors in which the airgap permeance is not constant. The cogging torque will cause undesirable speed pulsations, vibrations, possible resonance, and acoustic noise [10]. For the motor shown in Figure (1), because the radial and tangential components of the magnetic flux density vector, as presented in equation (11), are pure sinusoidal, the mmf harmonics only contain the fundamental component, and the cogging torque is caused by stator slots. In fact, the cogging torque can also be calculated by equation (17); however, $H_{\text{II}r}$ and $H_{\text{II}\theta}$ should be replaced by $H_{\text{II}r}^{\text{PM}}$ and $H_{\text{II}\theta}^{\text{PM}}$, respectively. In the paper, $H_{\text{II}r}^{\text{PM}}$ and $H_{\text{II}\theta}^{\text{PM}}$ are obtained by the hypothesis of a smooth stator surface; hereupon, they cannot reveal the slot effects. However, slot effects can be considered analytically by the subdomain technique. Works in the literature [10] have proposed a simple method to predict the

cogging torque based on the analytical calculation of the air-gap field distribution and the net lateral force acting on the teeth.

2.4. Back-Electromotive Force. The flux through a phase winding excited by PM and by winding, respectively, can be written as follows:

$$\begin{cases} \Phi_{\text{pm}} = \dfrac{2\left(B_{\text{IIr}}^{\text{PM}}\right)_{\max}}{\pi}\tau_p l_{\text{ef}}, \\ \\ \Phi_W = \dfrac{2\left(B_{\text{IIr}}^{W}\right)_{\max}}{\pi}\tau_p l_{\text{ef}}, \end{cases} \tag{19}$$

where τ_p is the pole pitch and l_{ef} is the length of stator iron. The back-emf amplitude in each phase winding, assuming a 120-degree coil span, is then obtained as follows:

$$E = 4.44 f k_{\text{dpv}} N \Phi_{\text{load}}, \tag{20}$$

where f is the angular frequency of the rotor, k_{dpv} is the winding coefficient, N is the number of turns per phase, and $\Phi_{\text{load}} = \Phi_{\text{pm}} + \Phi_W$. When $\Phi_W = 0$, it corresponds to an open-circuit situation, and the back-emf becomes the no-load back-emf E_0.

2.5. Armature Reaction Inductance. The constant-power transformation from the three-phase coordinates to the d-q coordinate is given by the following:

$$\begin{bmatrix} i_d \\ i_q \\ i_0 \end{bmatrix} = \sqrt{\frac{2}{3}} \begin{bmatrix} \cos\theta & \cos\left(\theta - \dfrac{2\pi}{3}\right) & \cos\left(\theta + \dfrac{2\pi}{3}\right) \\ -\sin\theta & -\sin\left(\theta - \dfrac{2\pi}{3}\right) & -\sin\left(\theta + \dfrac{2\pi}{3}\right) \\ \sqrt{\dfrac{1}{2}} & \sqrt{\dfrac{1}{2}} & \sqrt{\dfrac{1}{2}} \end{bmatrix} \begin{bmatrix} i_A \\ i_B \\ i_C \end{bmatrix}, \tag{21}$$

where $\theta = \int \omega\, dt$ represents the rotor position, which is an angle between the d-axis and winding axis of phase A. When the above two axes coincide, $\theta = 0$. Whereupon, according to equation (21), there are

$$\begin{bmatrix} i_d \\ i_q \end{bmatrix} = [C] \begin{bmatrix} i_A \\ i_B \\ i_C \end{bmatrix}, \tag{22a}$$

$$\begin{bmatrix} i_A \\ i_B \\ i_C \end{bmatrix} = [C]^T \begin{bmatrix} i_d \\ i_q \end{bmatrix}, \tag{22b}$$

where $[C] = \sqrt{2/3}\begin{bmatrix} 1 & -1/2 & 1/2 \\ 0 & \sqrt{3}/2 & -\sqrt{3}/2 \end{bmatrix}$ and $[C]^T$ and $[C]^{-1}$ are transposed matrix and inverse matrix of $[C]$, respectively. Notably, there is $[C]^T = [C]^{-1}$. According to equation (22a), we have

$$\begin{cases} i_d = \sqrt{\dfrac{2}{3}}\left(i_A - \dfrac{1}{2} i_B - \dfrac{1}{2} i_C\right), \\ \\ i_q = \sqrt{\dfrac{2}{3}}\left(\dfrac{\sqrt{3}}{2} i_B - \dfrac{\sqrt{3}}{2} i_C\right). \end{cases} \tag{23}$$

$\theta = 0$, which means $P\omega t = 0$ in equation (7). Substituting (7) into equation (23) yields

$$\begin{cases} i_d = \sqrt{3}\, I_{\text{Rms}} \cos(\beta), \\ i_q = \sqrt{3}\, I_{\text{Rms}} \sin(\beta), \end{cases} \tag{24}$$

where I_{Rms} is the RMS of phase current, $I_{\text{Rms}} = I_m/\sqrt{2}$, and β denotes the electrical angle of the phase current vector beyond the d-axis. Let $\beta = 0$; by substituting equation (24) into equation (22b) to get the three-phase AC $[i_A, i_B, i_C]$, when the three-phase AC flows into the stator windings, it will generate the d-axis armature reaction field. Obviously, the stator iron saturation is most likely to occur when the direction of the armature reaction field is in line with that of the PM field; accordingly, we only consider this situation.

Denoting the inductance matrix in the *abc* coordinate system by

$$[L_{ABC}] = \begin{bmatrix} L_{AA} & L_{AB} & L_{AC} \\ L_{BA} & L_{BB} & L_{BC} \\ L_{CA} & L_{CB} & L_{CC} \end{bmatrix}. \tag{25}$$

The flux linkage in the *abc* coordinate system can be represented as

$$\begin{bmatrix} \lambda_A \\ \lambda_B \\ \lambda_C \end{bmatrix} = L_{ABC} \begin{bmatrix} i_A \\ i_B \\ i_C \end{bmatrix}. \tag{26}$$

The flux linkage in the dq coordinate system is also applied to equation (22a), that is,

$$\begin{bmatrix} \lambda_d \\ \lambda_q \end{bmatrix} = [C] \begin{bmatrix} \lambda_A \\ \lambda_B \\ \lambda_C \end{bmatrix}. \tag{27}$$

Substituting equation (26) and equation (22b) into equation (27) yields the following:

$$\begin{bmatrix} \lambda_d \\ \lambda_q \end{bmatrix} = [C][L_{ABC}][C]^T \begin{bmatrix} i_d \\ i_q \end{bmatrix} = [L_{dq}] \begin{bmatrix} i_d \\ i_q \end{bmatrix}, \tag{28}$$

where $[L_{dq}] = \begin{bmatrix} L_d & L_{md} \\ L_{mq} & L_q \end{bmatrix} = [C][L_{ABC}][C]^T$; it represents the inductance matrix in the dq coordinate system. If the end leakage is not considered and other leakage factors such as higher harmonics and slot are also ignored, then L_d and L_q will represent the d-axis and q-axis armature reaction inductances, namely, L_{ad} and L_{aq}, respectively. From the FEM, $[L_{ABC}]$ will be obtained, and then it will turn into $[L_{dq}]$ by using the above transformation.

L_{ad} and L_{aq} can also be calculated by analytical method, and the process is as follows.

The load flux linkage of phase A is calculated as

$$\lambda_A = NR_2 l_{\text{ef}} \int_{-\alpha_y/2}^{\alpha_y/2} B_{\text{IIr}}^{\text{load}}(R_2, \theta) d\theta, \tag{29}$$

where N is the number of turns per coil of one phase winding and α_y is the coil pitch angle. The load flux linkage of phase B and C is expressed as

$$\begin{cases} \lambda_B = \lambda_A \cos \dfrac{2\pi}{3}, \\ \lambda_C = \lambda_A \cos \dfrac{4\pi}{3}. \end{cases} \tag{30}$$

According to the above-mentioned $[\lambda_A, \lambda_B, \lambda_C]$, from equation (27), we will get $[\lambda_d, \lambda_q]$. And then, there is

$$L_d = \frac{\lambda_d}{i_d}. \tag{31}$$

Similarly, neglecting some leakage factors, L_d calculated by equation (31), corresponds to L_{ad}.

3. Example Validation

To verify the analytic solution to the electromagnetic torque, a locked-rotor simulation is carried out by the FEM method. The motor parameters are listed in Table 1.

In the simulation, the windings are fed by a symmetrical three-phase alternating current to produce a rotating armature reaction field, but the rotor speed is set to zero; that is, the rotor is locked. When the armature reaction field rotates relative to the rotor with the angular velocity ω, the locked-rotor torque will generate and vary periodically with δ (an angle between two axes of the armature reaction field and PM field, and it changes periodically from 0 to 360 degrees). The locked-rotor phenomenon can be applied to verify the electromagnetic torque of equation (16) and equation (18).

When the motor is fed with currents as shown in equation (7), the locked-rotor torques are as shown in Figure 3. Three kinds of input currents of 2000 Hz with different amplitudes, such as 10 A, 30 A, and 50 A are considered. Figure 3(a) shows the three-phase currents with a 10 A peak value in FEM. The locked-rotor torque curves obtained by FEM are shown in Figure 3(b), which shows that the locked-rotor torque is also sinusoidal with time, and its peak value is increased with the increasing amplitude of the phase current. A comparison of the results of FEM and the analytical model is illustrated in Figure 3(c), in which it can be found that the analytical solution is in good agreement with the FEM solution.

Peak torques obtained by the FE model are compared with those from the derived analytical equations. The results, which are listed in Table 2, show that the errors are less than 5%, which proves the correctness of equation (16) and equation (18).

The magnetic field results that were calculated by FEM are shown in Figure 4, where red and blue conductors indicate the current flows out of and into the cross section, respectively. In addition, the PM has a parallel magnetization (the direction of the magnetization is vertically upward).

Table 1: Parameters of the high-speed PMSM.

Symbol	Quantity	Values
R_1	PM radius	12×10^{-3} m
R_2	Inner radius of stator	17.4×10^{-3} m
Q	Slot numbers	12
l_{ef}	Core length	55×10^{-3} m
M	Magnetization	820000 A/m
ω	Angular velocity	12560 rad/s
N_s	Conductors per slot	20
μ_r	Relative recoil permeability	1.038
P	Number of pole pairs	1

Because the PM field is much larger than the armature reaction field, the magnetic fields of the motor in Figure 4 at different times are approximately the same. At 0.2 ms, the locked-rotor torque in Figure 3(b) is negative, and the corresponding motor magnetic field is shown in Figure 4(a), in which the armature reaction field lags behind the PM field by approximately 135 degrees, which just causes a negative torque. Moreover, the armature reaction field weakens the PM field, the maximum flux density occurs in the stator tooth, and its value is 1.38 T. At 0.4 ms, the locked-rotor torque equals zero, as shown in Figure 3(b), and the corresponding motor magnetic field is shown in Figure 4(b), where the armature reaction field coincides with the PM field, which verifies the null torque. At 0.4 ms, the maximum flux density of the stator tooth is 1.70 T. At 0.5 ms, the locked-rotor torque approaches the maximum, as shown in Figure 3(b), and the corresponding motor magnetic field is shown in Figure 4(c). It can be seen that the armature reaction field direction is left (90 degrees ahead of the PM field), which verifies the maximum torque. At 0.5 ms, the maximum flux density of the stator tooth is 1.60 T.

Three methods, namely, the FM method, the air-gap permeance method [10], and the subdomain method, were used to estimate the cogging torque, and the results are shown in Figure 5. The air-gap permeance method is based on the assumption that the flux crosses the magnet and air gap in a straight line wherever a magnet faces a tooth. However, the above assumption will no longer be suitable for the motor mentioned in the paper, because the flux will bend in the air gap, as shown in Figure 5(a); the cogging torque calculated by the air-gap permeance method is small relative to that from FEM and the subdomain method, as shown in Figure 5(b). The cogging torque peak is approximately 370 μNm and is 0.05% of the rated torque (0.8 Nm), which is too small to be ignored. In fact, some degrees of harmonic components will exist in the polarized PM; thus, the cogging torque peak will increase.

The stator tooth tips in relation to the width of the slot openings also influence the back-emf waveform. When the height of the tooth tips is small, magnetic saturation exists and the emf waveform tends to be a trapezoid. However, when the tooth tip height is too large, the emf waveform will deteriorate [11]. The motor consists of a stator having 12

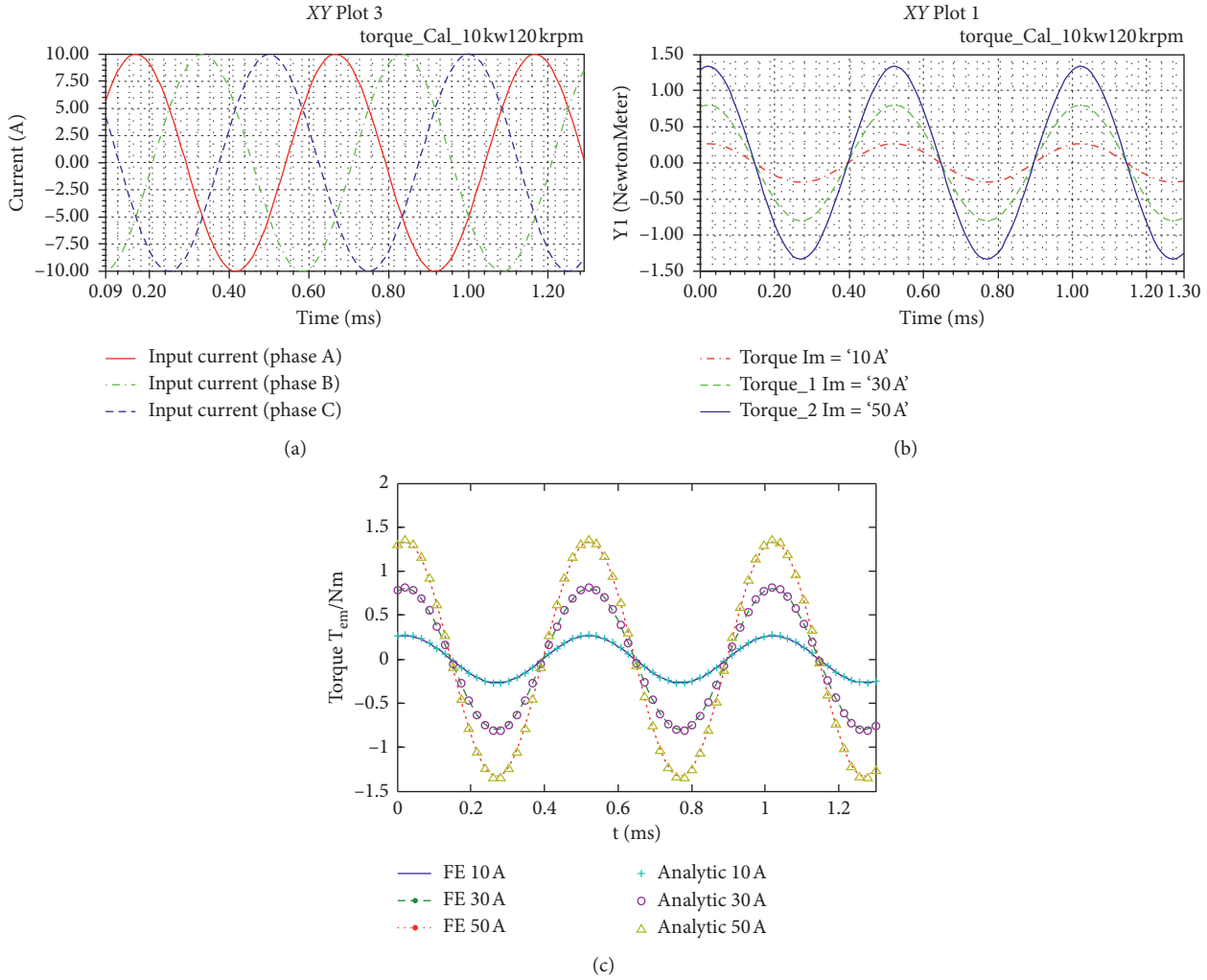

Figure 3: The results of the locked-rotor. (a) The three-phase alternating currents. (b) The torque vs time. (c) Result comparison of FEM and the analytical model.

Table 2: Peak torque comparison between FE and the theory.

I_m (A)	FEM (N·m)	Analytical (N·m)	Error (%)
10	0.266	0.271	1.87
30	0.802	0.815	1.62
50	1.333	1.357	1.76

teeth, which carry overlapping winding. The no-load back-emf waveform obtained from the FEM is displayed in Figure 6(a), and the emf waveform is almost purely sinusoidal, which is ideal for ultra-high-speed PMSMs. As shown in Figure 5(a), a stator tooth has the maximum flux density, 1.542 T, which does not reach the saturation region of the material. The comparison of the no-load back-emf calculated by equation (20) and that of FEM is shown in Figure 6(b), which manifests a good agreement of both methods. Figure 6(c) shows the prototype of the PMSM, in which the rotor is supported by gas foil bearings, and the experimental results are shown in Figure 6(d). A coast-down test under 60,000 r/min is carried out; that is, the frequency converter will shut down when the rotor is stable at 60,000 r/min, and then the rotor speed will decrease to zero gradually by overcoming air friction. In this process, the stator has a back-emf, but no current; thereupon, the rotor is not subjected to the electromagnetic force. Hereupon, the curve of a no-load back-emf vs speed can be achieved. The experimental and design values of the no-load back-emf are 57.0 V and 59.6 V at 746 Hz, respectively, and the difference between them is within 4.6%.

The results of L_{ad} and L_{aq} are shown in Figure 7. It can be found that L_{ad} and L_{aq} are same when current is small, and both of them decrease with the increase of the current. Because the d-axial magnetic circuit is more saturated, L_{ad} descends faster. The magnetic saturation is neglected in the analytical method, whereas L_{ad} not varies with the current.

When $I_{\mathrm{Rms}} = 10$ A and 100 A, the errors of the two methods are 9% and 2%, respectively. It shows that the results of the analytical method and FEM are very close. In the analytical method, only the fundamental harmonic is used to calculate the flux linkage. However, in the FEM, except for the fundamental harmonic, high-order harmonics

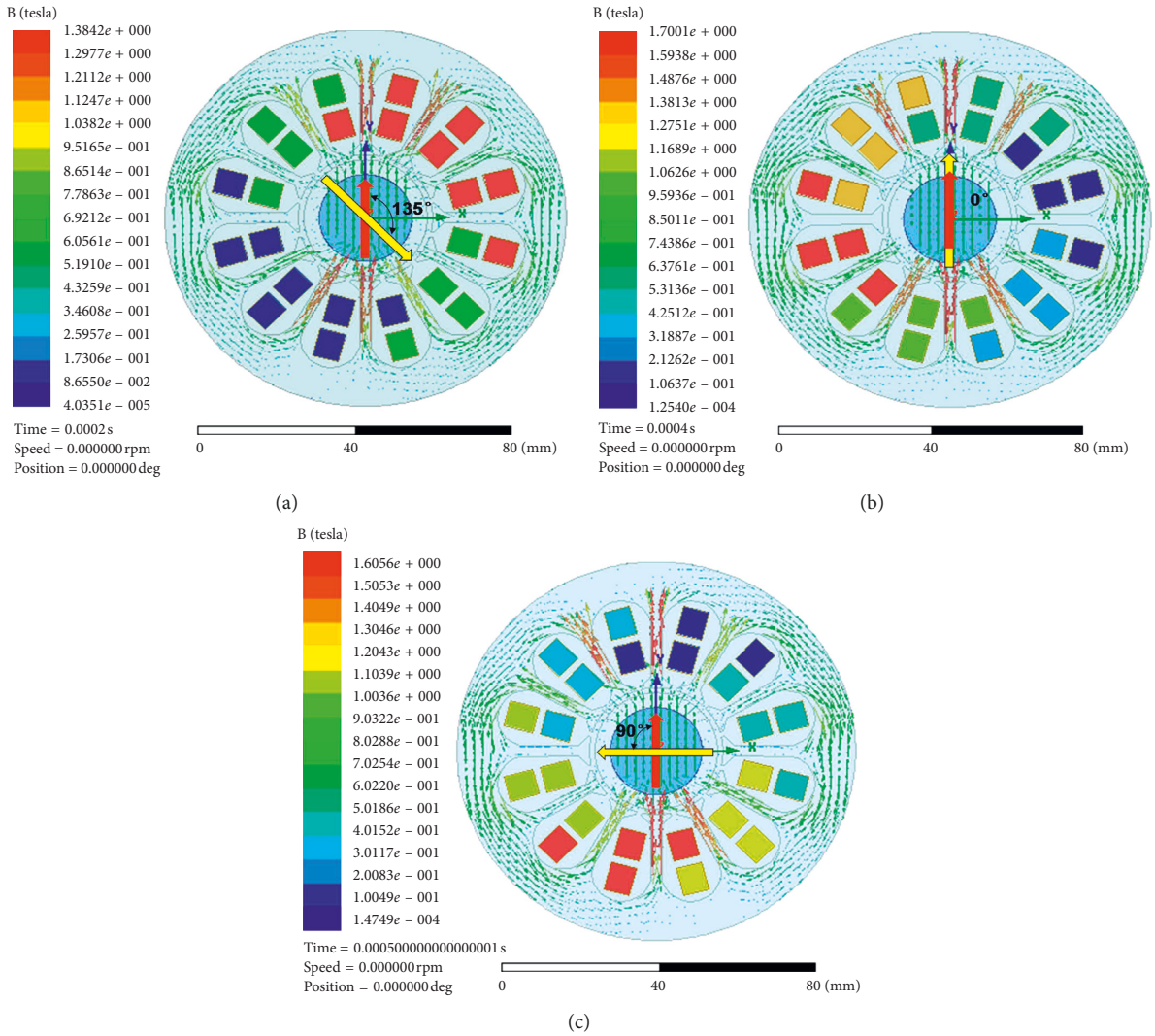

Figure 4: Flux density vector field and current vector field of the FE model. (a) Fields at 0.0002 s. (b) Fields at 0.0004 s. (c) Fields at 0.0005 s.

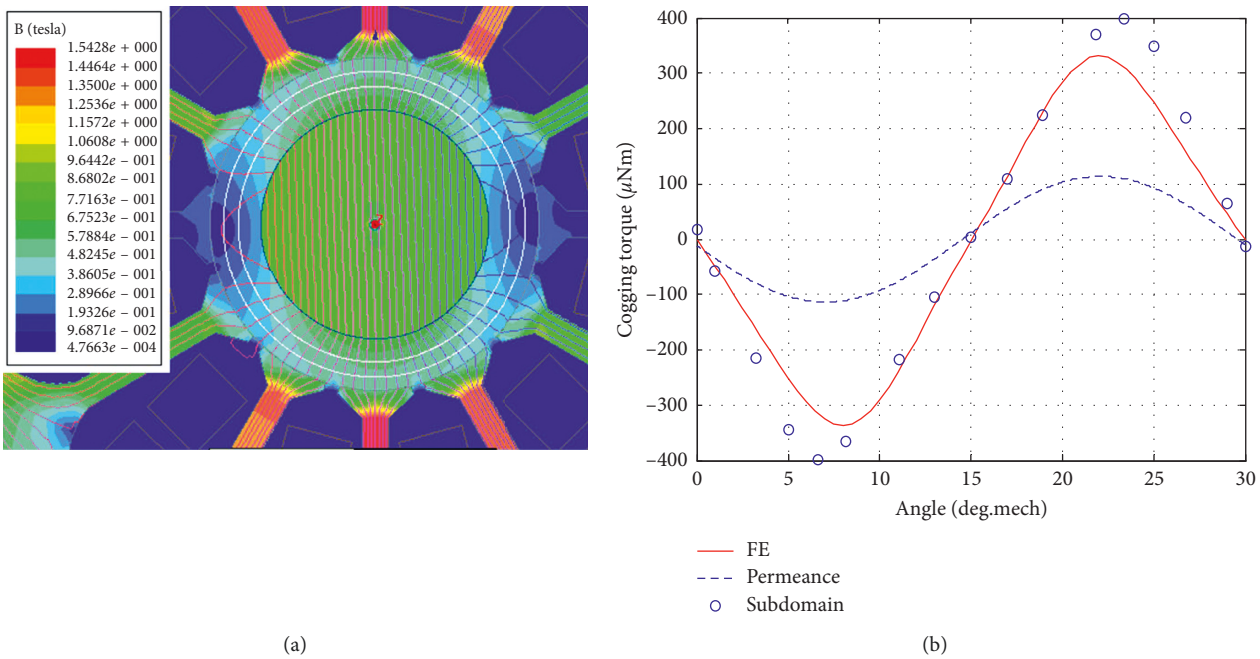

Figure 5: PM field and cogging torque. (a) PM field. (b) Comparison of the cogging torque of FEM and the analytical model.

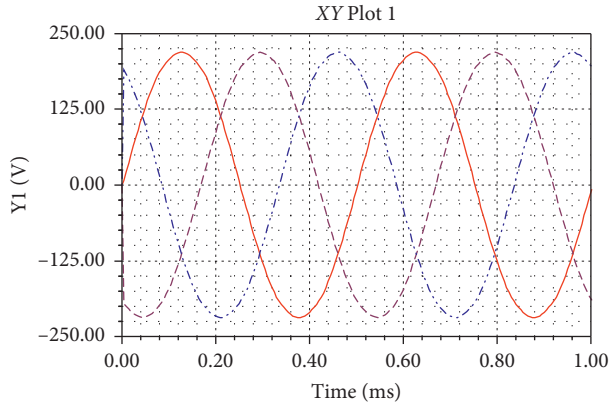

Curve info	rms_1	max
Induced voltage (phase A)	156.0441	218.8502
Induced voltage (phase B)	156.3378	218.6613
Induced voltage (phase C)	157.3086	218.4715

(a)

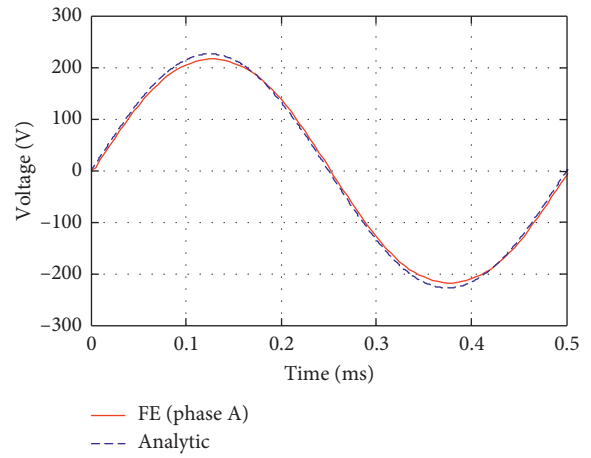

(b)

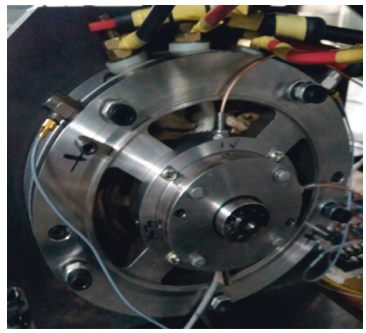

(c)

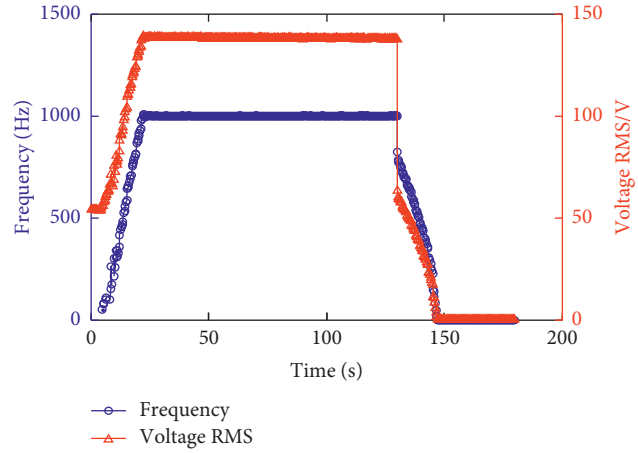

(d)

Figure 6: Results of the no-load back-emf. (a) No-load back-emf of FEM at 120,000 rpm. (b) Comparison of no-load back-emf at 120,000 rpm. (c) Prototype of the ultra-high-speed PMSM. (d) Experimental curves of the phase voltage and frequency.

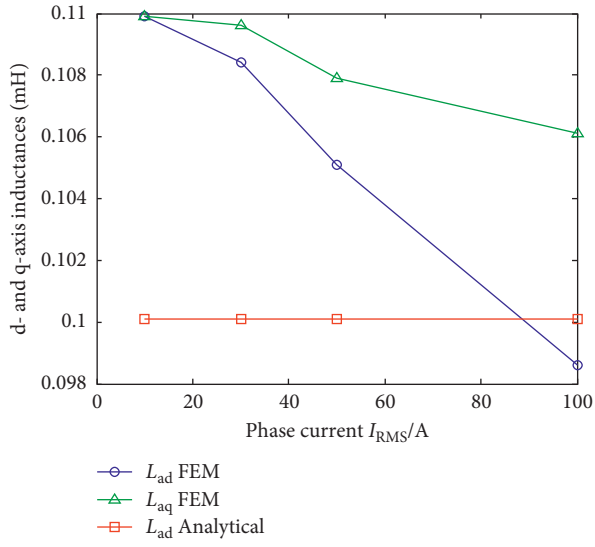

Figure 7: Curves of L_{ad} and L_{aq} vs the current.

are also taken into account in the flux linkage. Therefore, the result of the analytical method is smaller than that of FEM.

It is worth noting that the stator tooth has the most serious saturation as shown in Figure 8(a), and the flux densities reach 2.086 T and 1.880 T, when $I_{\mathrm{Rms}} = 100$ A ($2.8I_N$) and 50 A ($1.4I_N$), respectively. I_N denotes the rated current of the motor. The working points of stator tooth corresponding to the both working condition are illustrated in Figure 8(b). It shows that the working point is located at the end of the linear segment of the B-H curve when $I_{\mathrm{Rms}} = 1.4I_N$. It indicates that the magnetic saturation of the stator iron is not prominent when the prototype works under rated working conditions, and it applies to the proposed analytical method in this paper.

In addition, in order to enhance the cooling of the rotor, the air gap should be chosen as large as possible, so that magnetic saturation in the tooth tips rarely occurs. Furthermore, the teeth in a 12-slot stator are diametrically symmetrical, the air-gap field distribution is symmetrical,

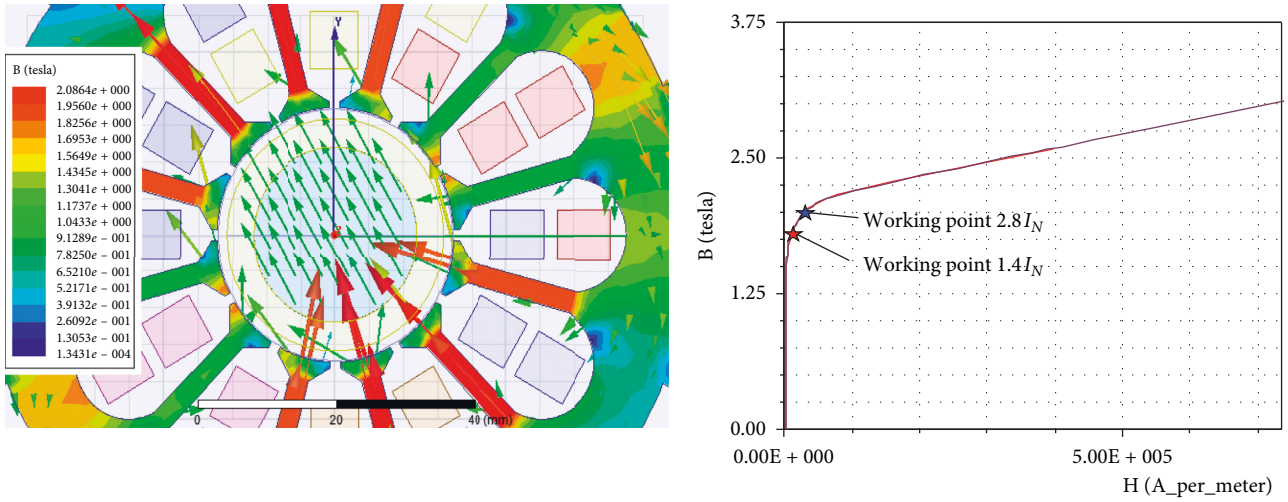

(a) (b)

Figure 8: Magnetic saturation condition of the stator iron. (a) Distribution of flux density for $I_{\mathrm{Rms}} = 100$ A. (b) Working points of the stator tooth.

and no unbalanced magnetic pull will exist if the rotor and stator axes are coincident. Although the rotor rotates eccentrically with respect to the stator, in fact, the eccentricity is too tiny due to the constraint of bearings to cause a notable unbalanced magnetic pull.

4. Conclusion

For the ultra-high-speed PMSM, including a stator with overlapping windings and the 2-pole parallel magnetized cylindrical PM, electromagnetic torques are rarely reported at present, which leads to a prolonged motor design cycle to evaluating motor performance. Therefore, the work of this paper is as follows:

(1) This paper deduces the analytical solution to the electromagnetic driving torque of ultra-high-speed PMSMs, which is verified by the FE method according to locked-rotor simulation. The results show that the electromagnetic torque is proportional to the length of stator iron, the ampere turns per unit length of the stator inner surface and the magnetization, while it is proportional to the square of the ratio, i.e., PM radius to stator inner radius.

(2) The cogging torque, back-emf, armature reaction inductance, and so on are calculated, compared, and discussed. For the PMSM studied in the paper, the air-gap permeance method was shown not to be applicable to the estimation of the cogging torque due to the fact that the flux bends in the air gap, and thus, a high-accuracy method (e.g., the subdomain method) should be adopted.

(3) A prototype is designed and manufactured, and the no-load back-emf is checked by a 60,000 rpm free coast experiment. The experimental and design values of the no-load back-emf are 57.0 V and 59.6 V at 746 Hz, respectively, and the difference between them is within 4.6%.

Data Availability

The data used to support the findings of this study are available from the corresponding author upon request.

Conflicts of Interest

The authors declare that they have no conflicts of interest.

Acknowledgments

This work is supported by National Natural Science Foundation of China (Grant nos. 51705413, 51705416, and 11502196) and China Postdoctoral Science Foundation (Grant no. 2017M613291XB).

References

[1] A. Tenconi, S. Vaschetto, and A. Vigliani, "Electrical machines for high-speed applications: design considerations and tradeoffs," *IEEE Transactions on Industrial Electronics*, vol. 61, no. 6, pp. 3022–3029, 2014.

[2] J. H. Ahn, J. Y. Choi, C. H. Park, C. Han, C. W. Kim, and T. G. Yoon, "Correlation between rotor vibration and mechanical stress in ultra-high-speed permanent magnet synchronous motors," *IEEE Transactions on Magnetics*, vol. 53, no. 11, Article ID 8209906, 2017.

[3] M.-S. Lim, S.-H. Chai, J.-S. Yang, and J.-P. Hong, "Design and verification of 150 krpm PMSM based on experiment results of prototype," *IEEE Transactions on Industrial Electronics*, vol. 62, no. 12, pp. 7827–7836, 2015.

[4] D.-K. Hong, B.-C. Woo, J.-Y. Lee, and D.-H. Koo, "Ultra high speed motor supported by air foil bearings for air blower cooling fuel cells," *IEEE Transactions on Magnetics*, vol. 48, no. 2, pp. 871–874, 2012.

[5] D.-K. Hong, B.-C. Woo, Y.-H. Jeong, D.-H. Koo, and C.-W. Ahn, "Development of an ultra high speed permanent magnet synchronous motor," *International Journal of Precision Engineering and Manufacturing*, vol. 14, no. 3, pp. 493–499, 2013.

[6] S.-M. Jang, H.-W. Cho, and S.-K. Choi, "Design and analysis of a high-speed brushless DC motor for centrifugal compressor," *IEEE Transactions on Magnetics*, vol. 43, no. 6, pp. 2573–2575, 2007.

[7] D.-K. Hong, D.-S. Joo, B.-C. Woo, D.-H. Koo, and C.-W. Ahn, "Unbalance response analysis and experimental validation of an ultra high speed motor-generator for microturbine generators considering balancing," *Sensors*, vol. 14, no. 9, pp. 16117–16127, 2014.

[8] A. B. Proca, A. Keyhani, A. EL-Antably, W. Lu, and M. Dai, "Analytical model for permanent magnet motors with surface mounted magnets," *IEEE Transactions on Energy Conversion*, vol. 18, no. 3, pp. 386–391, 2003.

[9] F. Dubas, C. Espanet, and A. Miraoui, "An original analytical expression of the maximum magnet thickness in surface mounted permanent magnet motors," *The European Physical Journal Applied Physics*, vol. 38, no. 2, pp. 169–176, 2007.

[10] Z. Q. Zhu and D. Howe, "Analytical prediction of the cogging torque in radial-field permanent magnet brushless motors," *IEEE Transactions on Magnetics*, vol. 28, no. 2, pp. 1371–1374, 1992.

[11] Z. Q. Zhu, K. Ng, and D. Howe, "Design and analysis of high-speed brushless permanent magnet motors," in *Proceedings of the International Conference on Electrical Machines & Drives*, pp. 381–385, IET, Cambridge, UK, September 1997.

[12] W. Cheng, L. Yu, L. Huang, Y. Lv, L. Li, and Y. Sun, "Analytical solution to magnetic field distribution of a parallel magnetised rotor with cylindrical or ring-type permanent magnet," *IET Electric Power Applications*, vol. 9, no. 6, pp. 429–437, 2015.

[13] Z. Q. Zhu and D. Howe, "Instantaneous magnetic field distribution in brushless permanent magnet DC motors. II. Armature-reaction field," *IEEE Transactions on Magnetics*, vol. 29, no. 1, pp. 136–142, 1993.